Selective catalytic reduction of NO with NH₃ over iron titanate catalyst: Catalytic performance and characterization

Fudong Liu [a], Hong He [a,*], Changbin Zhang [a], Zhaochi Feng [b], Lirong Zheng [c], Yaning Xie [c], Tiandou Hu [c]

[a] State Key Laboratory of Environmental Chemistry and Ecotoxicology, Research Center for Eco-Environmental Sciences, Chinese Academy of Sciences, Beijing 100085, PR China
[b] State Key Laboratory of Catalysis, Dalian Institute of Chemical Physics, Chinese Academy of Sciences, Dalian 116023, PR China
[c] Institute of High Energy Physics, Chinese Academy of Sciences, Beijing 100049, PR China

ARTICLE INFO

ABSTRACT

A novel iron titanate catalyst prepared by conventional co-precipitation method showed excellent activity, N_2 selectivity and H_2O/SO_2 durability in the selective catalytic reduction (SCR) of NO with NH_3. The influence of precursors and preparation methods on the catalyst structure and activity was comprehensively investigated. Iron titanate catalyst prepared using titanium sulfate as Ti precursor was favorable for the high activity and selectivity, comparing with that using titanium tetrachloride as precursor and Fe_2O_3/TiO_2 loaded type catalyst. Especially, the best iron titanate catalyst showed good activity in a temperature window of 200–350 °C with the NO_x conversion above 90% in the absence of H_2O, which was 50–150 °C lower than those of other known Fe-based catalysts. Iron titanate crystallite with specific Fe–O–Ti structure was found to be the main active phase. The interaction between iron and titanium species in atomic scale led to an enhancement of oxidative ability of Fe^{3+}, which was beneficial to the SCR reaction.

1. Introduction

Selective catalytic reduction (SCR) of NO with NH_3 has been an efficient and economic technique for the removal of NO_x from exhaust gases of stationary and mobile sources, such as coal fired power plants and lean-burn diesel engines. Nowadays, the most widely used catalyst system is V_2O_5–WO_3 $(MoO_3)/TiO_2$ which still shows some actual problems, such as the low N_2 selectivity in high temperature range owing to the formation of N_2O, the high conversion of SO_2 to SO_3 [1], and the toxicity of vanadium pentoxide to environment and human health (such as causing irritation to skin, eyes and respiratory tract) [2]. Therefore, a lot of studies have been performed to find new SCR catalyst systems which probably can be used to substitute the conventional vanadium-based catalyst [3–8]. Among them, Fe-based catalysts usually showed good SCR activity and N_2 selectivity in the relatively high temperature range.

In general, most of the Fe-based catalysts are Fe^{3+}-exchanged zeolites or Fe_2O_3 loaded types, such as Fe/ZSM-5 [6], Fe^{3+}-exchanged TiO_2-pillared clay [7], Fe_2O_3–WO_3/ZrO_2 [8] and Fe_2O_3/TiO_2 [9]. TiO_2 is usually used as the support of SCR cata-

lysts due to its excellent SO_2 durability, because TiO_2 essentially reacts with neither SO_3 nor SO_2 above 200 °C [10]. Based on the idea of combining the advantages of Fe-based catalysts and TiO_2 support, in our previous work [11] we presented an environmentally friendly novel iron titanate catalyst prepared by co-precipitation method which showed excellent SCR activity, N_2 selectivity and H_2O/SO_2 durability in the medium temperature range (200–400 °C). Comparing with the similarly environmentally friendly Fe-zeolite SCR catalysts which are bringing commercialized in the US, the low temperature SCR activity of this iron titanate catalyst was much higher. We deduced that the iron titanate crystallite, but not the aggregated iron oxides, was the main active phase in the SCR process; however, the evidences were not sufficient and the catalytic mechanism was unclear, either. In this work, we comprehensively characterized this iron titanate catalyst using various techniques, and also investigated the influence of different precursors and preparation methods on the structure and activity. Parametric experiments were also conducted to test the durability of high space velocity and high reactant concentration over this catalyst, which was important for the actual industrial use. The redox behaviors of iron and titanium species in this catalyst were also examined using H_2-temperature programmed reduction (H_2-TPR) and X-ray photoelectron spectra (XPS) methods. Based on the understanding of the relationship between catalyst structure and catalytic activity, the SCR mechanism over this iron titanate catalyst will be discussed in detail in the successive series of this study.

* Corresponding author. Postal address: P.O. Box 2871, 18 Shuangqing Road, Haidian District, Beijing 100085, PR China. Tel.: +86 10 62849123; fax: +86 10 62849123.
E-mail address: honghe@rcees.ac.cn (H. He).

2. Experimental

2.1. Catalysts synthesis

The iron titanate catalysts (Fe_xTiO_y) were synthesized by co-precipitation method using $TiCl_4$ or $Ti(SO_4)_2$ as Ti precursor and $Fe(NO_3)_3 \cdot 9H_2O$ as Fe precursor with the molar ratio of Fe:Ti = 1:1. When using $TiCl_4$ as Ti precursor, it was firstly diluted with ice-cold distilled water in the bath of ice-water mixture avoiding intense hydrolysis to prepare a known concentration of $TiOCl_2$ solution. Because of the slow hydrolysis of $TiCl_4$ at low temperature, no TiO_2 precipitation occurred during the preparation process of $TiOCl_2$ solution. Then a stoichiometric amount of $Fe(NO_3)_3$ solution was added in with subsequent stirring for 1 h without the formation of any precipitation in this process, either. Afterwards, standard $NH_3 \cdot H_2O$ (25 wt.%) was used as precipitator until the pH rose to 10 when the Fe and Ti ions were completely co-precipitated. Without aging, the precipitate was filtrated and washed, followed by desiccation at 100 °C for 12 h and calcination at 400 °C for 6 h in air. The calcined sample was crushed and sieved to 20–40 mesh for activity tests, and sieved powder above 120 mesh was used for characterizations. Catalyst prepared from $TiCl_4$ was denoted as Fe_xTiO_y–$TiCl_4$. When using $Ti(SO_4)_2$ as Ti precursor, $TiOSO_4$ solution could be obtained more easily because the hydrolysis of $Ti(SO_4)_2$ was much slower than that of $TiCl_4$. $Ti(SO_4)_2$ and $Fe(NO_3)_3 \cdot 9H_2O$ were firstly dissolved together with distilled water without the formation of any precipitation, and the rest procedures were controlled exactly the same as those of Fe_xTiO_y–$TiCl_4$. Catalyst prepared from $Ti(SO_4)_2$ was denoted as Fe_xTiO_y–$Ti(SO_4)_2$. Pristine Fe_2O_3 and TiO_2 as reference materials were prepared using $Fe(NO_3)_3 \cdot 9H_2O$ and $Ti(SO_4)_2$ as precursors, respectively. We also prepared Fe_2O_3/TiO_2 loaded type catalyst (Fe:Ti = 1:1 in molar ratio) using conventional impregnation method for comparison.

2.2. Activity test and in situ diffuse reflectance infrared Fourier transform spectroscopy of NO oxidation

The NH_3-SCR activity tests were carried out in a fixed-bed quartz tube reactor at atmospheric pressure. The flue gas was simulated by blending different gaseous reactants, including 500 ppm NO, 500 ppm NH_3, 5 vol.% O_2 and balance N_2. Catalyst used in each experiment was 0.6 ml and the total flow rate was 500 ml/min, yielding a gas hourly space velocity (GHSV) of 50,000 h^{-1}. Because of the density difference, in the SCR activity test ca. 0.4 g Fe_xTiO_y–$Ti(SO_4)_2$, 0.6 g Fe_xTiO_y–$TiCl_4$ and 0.35 g Fe_2O_3/TiO_2 were used to obtain the consistent GHSV. The separate NO oxidation activity was tested when NH_3 was not supplied, and the separate NH_3 oxidation activity was tested when NO was not provided. The influence of NO_2 inlet concentration on SCR activity was also investigated when the NO_2/NO_x molar ratio was adjusted to 25 and 50% by using homemade Cu_xTiO_y as NO pre-oxidation catalyst. Different reactant concentration experiments and oxygen concentration experiments were carried out by tuning the composing ratios of flue gas without changing the total flow rate. On the contrary, different GHSV experiments were carried out by tuning the total flow rate without changing the composing ratios of flue gas. The effluent gas was continuously analyzed by an FTIR spectrometer (Nicolet Nexus 670) equipped with a heated, low volume multiple-path gas cell (2 m). The spectra were collected three times for average after 60–120 min when the SCR process reached a steady state. It took 6–8 h to conduct each SCR reaction study, during which no degradation characteristic of catalysts was observed. During the reaction process, no other nitrogen-containing component besides of NO, NO_2, N_2O and NH_3 was detected in the flue gas, as shown in Supporting Information, Fig. S1. NO_x conversion (X_{NO_x})

and N_2 selectivity (S_{N_2}) were calculated as follows:

$$X_{NO_x} = \left(1 - \frac{[NO_x]_{out}}{[NO_x]_{in}}\right) \times 100\% \text{ with } [NO_x] = [NO] + [NO_2] \quad (1)$$

$$S_{N_2} = \left(\frac{[NO]_{in} + [NH_3]_{in} - 2[N_2O]_{out} - [NO_2]_{out}}{[NO]_{in} + [NH_3]_{in}} \times 100\%\right) \quad (2)$$

The in situ diffuse reflectance infrared Fourier transform spectroscopy (in situ DRIFTS) of NO oxidation over Fe_xTiO_y–$Ti(SO_4)_2$ and Fe_xTiO_y–$TiCl_4$ were performed on an FTIR spectrometer (Nicolet Nexus 670) equipped with an MCT/A detector cooled by liquid nitrogen. An in situ DRIFTS reactor cell with ZnSe window (Nexus Smart Collector) connected to a purging/adsorption gas control system was used. The reaction temperature was controlled precisely by an Omega programmable temperature controller. Prior to each experiment, the sample was pretreated at 400 °C in a flow of 20 vol.% O_2/N_2 for 30 min and then cooled down to the desired reaction temperature (200 °C). The spectra of catalyst at 200 °C were collected in flowing N_2 atmosphere and set as background, which was automatically subtracted from the final spectra. The total flow rate of the feeding gas was kept at 300 ml/min and all spectra were recorded by accumulating 100 scans with a resolution of 4 cm^{-1}. After 1 h reaction, the catalyst surface was purged by flowing N_2 for 30 min. The reaction conditions were controlled as follows: 500 ppm NO, 5 vol.% O_2 and N_2 balance.

2.3. Structural characterizations

N_2 adsorption–desorption isotherms of all samples were measured at −196 °C with a Quantachrome Autosorb-1C instrument. Prior to N_2 adsorption, the samples were degassed at 300 °C for 4 h. The surface areas were determined by BET equation in 0.05–0.35 partial pressure range. The pore volumes and pore size distributions were determined by BJH method from the desorption branches of the isotherms.

Powder X-ray diffraction (Powder XRD) measurements were carried out on a computerized Rigaku D/max-RB Diffractometer (Japan, Cu K_α as radiation resource). The data of 2θ from 10° to 90° were collected at 4°/min with the step size of 0.02°.

UV–vis diffuse reflectance spectroscopy (UV–vis DRS) were recorded on a JASCO V-550 UV–vis spectrophotometer equipped with an integrating sphere attachment (ISV4469) under ambient conditions. The spectra were collected in the wavelength range of 200–900 nm using $BaSO_4$ as reference material.

Visible Raman spectra were collected at room temperature on a Spex 1877 D triplemate spectrograph with spectral resolution of 2 cm^{-1}. A 532 nm DPSS diode-pump solid semiconductor laser was used as the excitation source and the power output was about 80 mW. UV Raman spectra were collected at room temperature on a homemade UV range specially designed Jobin-Yvon T64000 triple-stage Raman spectrograph with spectral resolution of 2 cm^{-1}. The laser line at 325 nm emitted from a KIMMON IK-3351R-G He–Cd laser was used as excitation source with a power output of 25 mW. Before measurements, the samples were well ground and mounted into a spinning holder to avoid thermal damage during the scanning. The Raman signals were collected with conventional 90° geometry and the time for recording each spectrum was about 5 min. All Raman spectra used in this paper were original and unsmoothed.

X-ray absorption fine-structure (XAFS) measurements were implemented on the 1W1B wiggler beam line of Beijing Synchrotron Radiation Facility (BSRF). The storage ring was operated at about 120 mA and 2.5 GeV. A fixed-exit Si(1 1 1) double-crystal monochromator was used to reduce the harmonic content of the monochrome beam. The incident and output beam intensities were monitored and recorded using ionization chambers filled by pure

nitrogen. Before XAFS measurement, the catalyst samples were crushed into fine powder above 200 mesh and coated onto transparent adhesive tapes. The absorption spectra (X-ray absorption near-edge spectroscopy, XANES and extended X-ray absorption fine-structure spectroscopy, EXAFS) of Fe K-edge and Ti K-edge in Fe_xTiO_y–$Ti(SO_4)_2$ were recorded in transmission mode at room temperature. The absorption spectra of Fe K-edge in Fe_2O_3 and Ti K-edge in TiO_2 were also recorded in the same mode as reference spectra. All spectra were collected at an interval of 0.7 eV in the XANES region and at an interval of 4 eV in the EXAFS region. XAFS data were analyzed using WinXAS software package [12]. The back-subtracted EXAFS function was firstly converted into k space and weighted by k^3 in order to compensate for the diminishing amplitude because of the decay of the photoelectron wave. The Fourier transforming of the k^3-weighted EXAFS data was performed in the range of $k = 2$–$13.44\,\text{Å}^{-1}$ for Fe K-edge and $k = 2.3$–$11.08\,\text{Å}^{-1}$ for Ti K-edge with a Hanning function window. In the least-square-fitting procedure, the possible scattering paths were calculated using IFEF-FIT software package [13].

2.4. Redox behavior characterizations

H_2-TPR experiments were carried out over Fe_xTiO_y–$Ti(SO_4)_2$ using Fe_2O_3 and TiO_2 as reference materials. The samples (100 mg) were firstly pretreated in a flow of 20 vol.% O_2/Ar (30 ml/min) at 300 °C for 30 min and then cooled down to the room temperature. In a flow of 5 vol.% H_2/Ar (30 ml/min), the temperature was raised linearly to 900 °C at the rate of 10 °C/min. The H_2 signal ($m/z = 2$) was monitored online using a quadrupole mass spectrometer (HPR20, Hiden Analytical Ltd.).

The XPS of Fe_xTiO_y–$Ti(SO_4)_2$, Fe_2O_3 and TiO_2 were recorded on a Scanning X-ray Microprobe (PHI Quantera, ULVAC-PHI, Inc.) using Al K_α radiation. The binding energies (Fe 2p, Ti 2p) were calibrated using C 1s peak (BE = 284.8 eV) as standard.

3. Results

3.1. Catalytic performance

3.1.1. SCR activity

Catalysts prepared with different precursors and preparation methods were tested for the NH_3-SCR reaction in the absence of H_2O (Fig. 1). The standard deviation of the calculated NO_x con-

Fig. 1. NO_x conversion and N_2 selectivity in the NH_3-SCR reaction over (a) Fe_xTiO_y–$Ti(SO_4)_2$, (b) Fe_xTiO_y–$TiCl_4$, and (c) Fe_2O_3/TiO_2. Reaction conditions: $[NO] = [NH_3] = 500$ ppm, $[O_2] = 5$ vol.%, N_2 balance and GHSV = 50,000 h^{-1}.

version and N_2 selectivity was also presented in the form of error bars. Fe_xTiO_y–$Ti(SO_4)_2$ showed the best activity and selectivity in a wide temperature range with NO_x conversion above 95% from 225 to 350 °C in the absence of H_2O, and the N_2 selectivity was always above 94% even at 400 °C. For practical utilization, the flue gases usually contain some volume fractions of water vapor, which may inhibit the low temperature SCR activity due to the blocking of active sites and enhance the high temperature SCR activity owing to the weakening of unselective oxidation of NH_3. Therefore, in the real SCR feeding streams the operation temperature window of this catalyst should shift towards the high temperature range to a certain extent. Similar effect of water vapor on SCR activity was observed over Mn substituted iron titanate catalyst developed in our lab [14]. Besides of the variation of SCR activity in the presence of H_2O, the SCR reaction pathway might also be changed, which can be studied in detail in our future work. Compared with Fe_xTiO_y–$Ti(SO_4)_2$, Fe_xTiO_y–$TiCl_4$ had a poor low temperature activity and a similar high temperature activity. If the W/F was kept the same in the SCR activity test, much higher NO_x conversions at low temperatures might be obtained over Fe_xTiO_y–$Ti(SO_4)_2$ than that over Fe_xTiO_y–$TiCl_4$. For Fe_2O_3/TiO_2, the low temperature activity was also much lower than that of Fe_xTiO_y–$Ti(SO_4)_2$, and the maximum NO_x conversion could not reach 100% together with poor N_2 selectivity above 300 °C.

3.1.2. NO and NH_3 oxidation activity

Previous study showed that increasing the NO_2/NO_x molar ratio in the feeding gas could significantly promote the low temperature activity over SCR catalysts [15,16]. The role of NO and NO_2 in the NO_x reduction process over Fe/ZSM-5 and V_2O_5–WO_3/TiO_2 was clearly elucidated, and the overall reaction was usually demonstrated as "fast SCR": $NO + NO_2 + 2NH_3 \rightarrow 2N_2 + 3H_2O$ [17,18]. In practical utilization, if the SCR catalysts could produce some fractions of NO_2 in situ from NO oxidation at low temperatures, the low temperature SCR activity would be enhanced accordingly due to the occurrence of "fast SCR" [19,20]. Therefore, the separate NO oxidation activity of our different catalysts was tested and the results are shown in Fig. 2A.

Within the accepted error range, in the relatively low temperature range below 250 °C the NO oxidation activity decreased in the following sequence: Fe_xTiO_y–$Ti(SO_4)_2$ > Fe_2O_3/TiO_2 > Fe_xTiO_y–$TiCl_4$, which is in well accordance with the sequence of low temperature SCR activity in Fig. 1. Although the amount of produced NO_2 in NO oxidation reaction was relatively small, the promoting effect of NO_2 formation in the SCR reaction was remarkable due to the continuous consumption of adsorbed NO_2 in the presence of reducing agent NH_3. In NO oxidation reaction without NH_3 adsorbed species on catalyst surface, the in situ formed nitrate species should go through decomposition to give out gaseous NO_2. At the same time, the in situ formed nitrate species would also play the role as NO_2 formation inhibitor if no reducing agent was supplied. However, in the real SCR reaction the in situ formed nitrate species could directly react with adsorbed NH_3 species to give out N_2. The surface reaction between nitrate species and NH_3 adsorbed species would dominate in the SCR reaction rather than nitrate decomposition. Therefore, it was reasonable to get slower NO_2 formation rate in separate NO oxidation reaction than the SCR reaction rate over different catalysts. For example, as the in situ DRIFTS of NO oxidation at 200 °C over Fe_xTiO_y–$Ti(SO_4)_2$ and Fe_xTiO_y–$TiCl_4$ shown in Fig. 3, much more surface nitrate species could form on Fe_xTiO_y–$Ti(SO_4)_2$ than that on Fe_xTiO_y–$TiCl_4$ under the same reaction conditions, including bridging nitrate at 1618–1624 cm^{-1} (ν_3 high) and 1196–1203 cm^{-1} (ν_3 low), bidentate nitrate at 1578–1579 cm^{-1} (ν_3 high) and monodentate nitrate at 1558–1560 cm^{-1} (ν_3 high) [5,21–23]. The small difference of NO oxidation ability would get

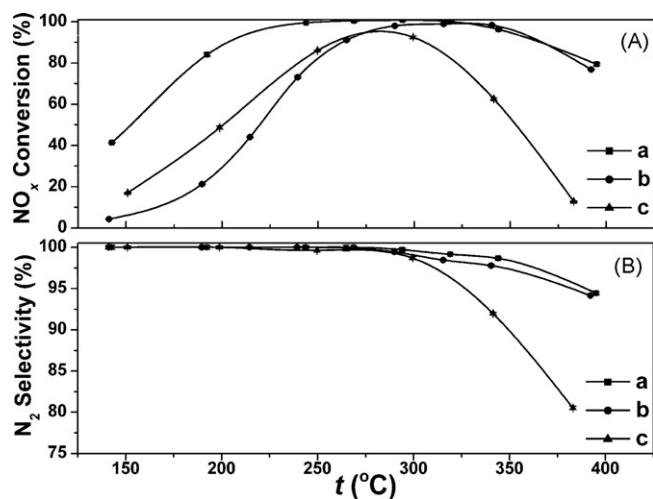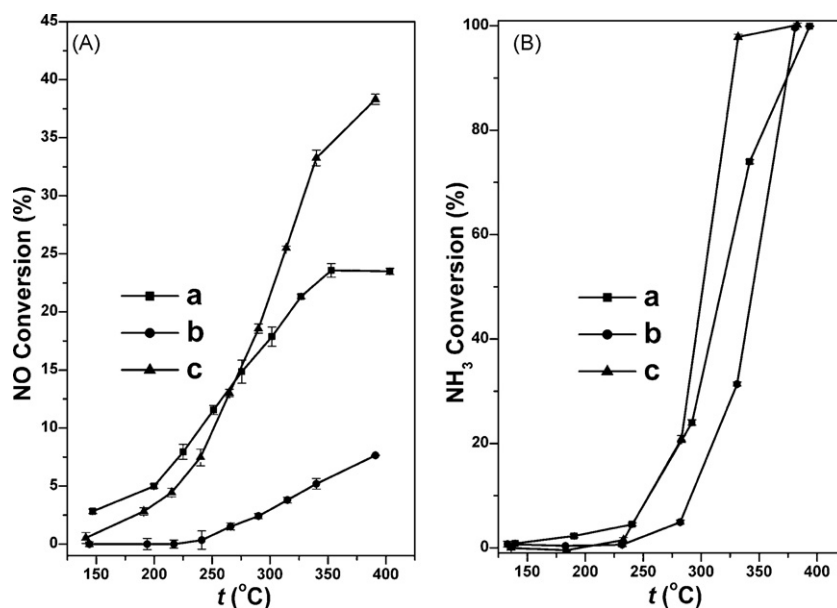**Fig. 2.** Separate NO oxidation activity (A) and separate NH_3 oxidation activity (B) over (a) Fe_xTiO_y–$Ti(SO_4)_2$, (b) Fe_xTiO_y–$TiCl_4$, and (c) Fe_2O_3/TiO_2. Reaction conditions: [NO] = 500 ppm or [NH_3] = 500 ppm, [O_2] = 5 vol.%, N_2 balance and GHSV = 50,000 h^{-1}.

amplified once the *in situ* formed nitrate species was continuously consumed in the reaction with reducing agent NH_3, leading to the large difference of SCR activity over these two catalysts at low temperatures.

Back to Fig. 2A, in the relatively high temperature range above 300 °C, Fe_2O_3/TiO_2 showed the highest NO conversion to NO_2, however the SCR activity over this catalyst was the lowest. It seems that the SCR activity in the relatively high temperature range cannot be simply associated with the NO oxidation activity, because during this process the unselective oxidation of NH_3 to NO_x may occur if the oxidative ability of SCR catalyst is too strong.

Afterwards, the separate NH_3 oxidation activity over our different catalysts was also measured and the results are shown in Fig. 2B. Similar as the NO oxidation activity above 300 °C, the NH_3 oxidation activity decreased in the following sequence:

Fe_2O_3/TiO_2 > Fe_xTiO_y–$Ti(SO_4)_2$ > Fe_xTiO_y–$TiCl_4$. The oxidative ability of Fe_2O_3/TiO_2 catalyst was indeed too strong at high temperatures, resulting in the competitive consumption of NH_3 in the formation of N_2O, NO or NO_2. Comparatively, the oxidative ability of Fe_xTiO_y–$Ti(SO_4)_2$ and Fe_xTiO_y–$TiCl_4$ was moderate, which is in accordance with their high temperature SCR activity and N_2 selectivity above 300 °C. Moreover, the study by Balle et al. [24] showed that under the SCR conditions, NH_3 oxidation was likely to be more suppressed on isolated iron sites than on agglomerated iron oxide sites. Therefore, although the NH_3 oxidation activity of Fe_xTiO_y–$Ti(SO_4)_2$ seemed to be higher than that of Fe_xTiO_y–$TiCl_4$, the high temperature SCR activity was similar probably because of more isolated iron sites over Fe_xTiO_y–$Ti(SO_4)_2$ than that over Fe_xTiO_y–$TiCl_4$. This point of view will be discussed in detail in the characterization sections. The best catalyst Fe_xTiO_y–$Ti(SO_4)_2$ was
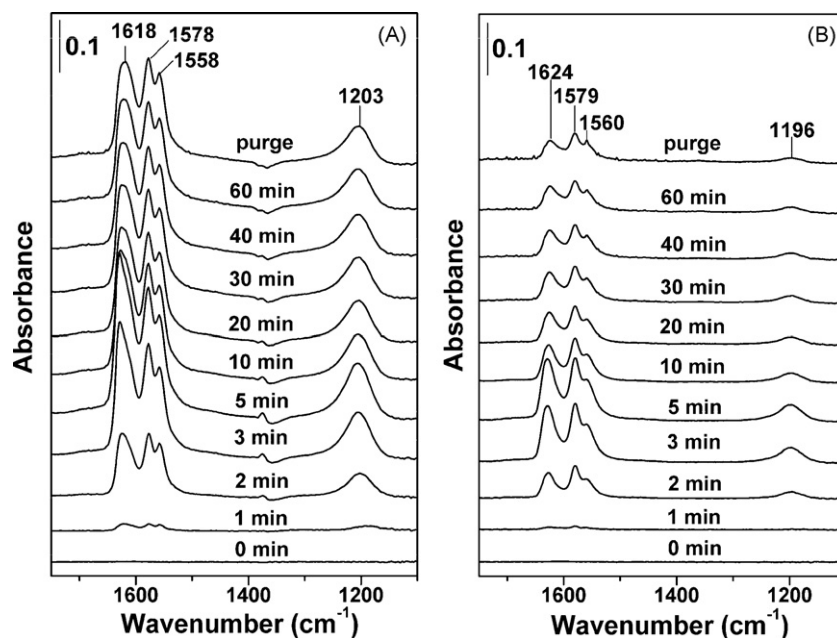

Fig. 3. *In situ* DRIFTS of NO oxidation over (A) Fe_xTiO_y–$Ti(SO_4)_2$ and (B) Fe_xTiO_y–$TiCl_4$ at 200 °C. Reaction conditions: [NO] = 500 ppm, [O_2] = 5 vol.% and N_2 balance.
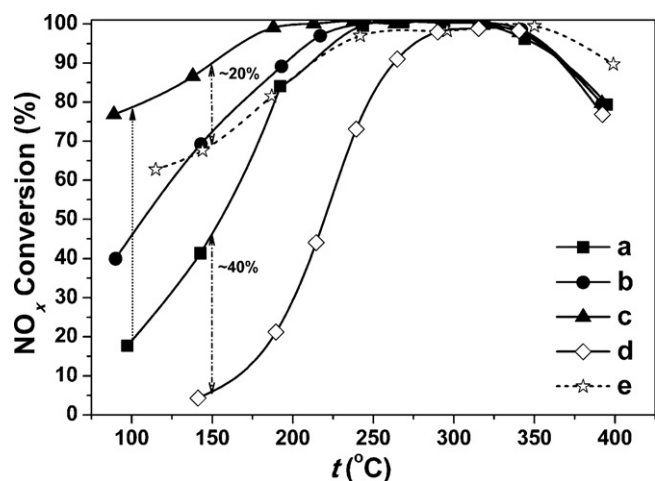
Fig. 4. NO_x conversion in the NH_3-SCR reaction over Fe_xTiO_y–$Ti(SO_4)_2$ with the molar NO_2/NO_x ratio of (a) 0%, (b) 25%, (c) 50% and over Fe_xTiO_y–$TiCl_4$ with the molar NO_2/NO_x ratio of (d) 0%, and (e) 50%. Reaction conditions: $[NO_x] = [NH_3] = 500$ ppm, $[O_2] = 5$ vol.%, N_2 balance and GHSV = 50,000 h^{-1}.

chosen as model catalyst for the following parametric experiments.

3.1.3. Effect of NO_2 inlet concentration on SCR activity

In order to further clarify the importance of "fast SCR" to the low temperature SCR activity, we also investigated the effect of NO_2 inlet concentration on NO_x conversion over Fe_xTiO_y–$Ti(SO_4)_2$ and Fe_xTiO_y–$TiCl_4$ by tuning the molar NO_2/NO_x ratio to 25 and 50% (Fig. 4, error bars not shown afterwards because of small standard deviations). Over Fe_xTiO_y–$Ti(SO_4)_2$, with the increasing of NO_2 inlet concentration the NO_x conversion below 200 °C showed a drastic increase, e.g. from 18% (0% NO_2) to 45% (25% NO_2) and 78% (50% NO_2) at 100 °C (as shown by the dotted arrow). The similar results were also observed over other iron-containing SCR catalysts, such as Fe/ZSM-5 and Fe/HBEA [15,24]. Over Fe_xTiO_y–$TiCl_4$, when the NO_2/NO_x ratio was adjusted to 50%, the low temperature SCR activity was also greatly enhanced. Smaller difference of NO_x conversion (ca. 20%) below 200 °C between Fe_xTiO_y–$Ti(SO_4)_2$ and Fe_xTiO_y–$TiCl_4$ was obtained under this reaction condition, in

contrast to the relatively large NO_x conversion difference at ca. 40% when the NO_2/NO_x ratio was 0% (as shown by the double-head arrows). This means that, taking no account of other factors to influence the SCR activity such as surface area and acidity, etc., the Fe_xTiO_y–$Ti(SO_4)_2$ catalyst lost some of its advantage when the in situ NO oxidation was no longer a limiting step in the SCR reaction. In short summary, the proper molar ratio of NO_2/NO_x in the feeding gas or the improved in situ NO oxidation functionality of iron-containing catalysts is required to enhance their low temperature SCR activity.

3.1.4. Effects of GHSV and reactant concentration on SCR activity

Typical GHSV of exhaust from power plant is usually higher than 30,000 h^{-1} [25] and the GHSV of exhaust from vehicles under different working conditions usually differ a lot, thus the influence of GHSV on NO_x conversion was investigated over Fe_xTiO_y–$Ti(SO_4)_2$ (Fig. 5A). With the GHSV increasing from 25,000 to 250,000 h^{-1}, NO_x conversion had an obvious decline in the relatively low temperature range, and the maximum value also decreased from 100 to 88%. NO_x concentration in the exhaust from stationary and mobile sources also changes with working conditions, thus the influence of reactant concentration on NO_x conversion was also studied by keeping the ratio of $NO:NH_3:O_2 = 1:1:100$ (Fig. 5B). With the NO and NH_3 concentration increasing from 200 to 1000 ppm and O_2 concentration increasing from 2 to 10 vol.%, the NO_x conversion had a slight decrease in the low temperature range (150–200 °C) and an obvious increase in the high temperature range (350–400 °C). The maximum NO_x conversion could reach 100% under all reaction conditions.

3.1.5. Effect of oxygen concentration on SCR activity

Previous studies have shown that O_2 played an important role in the NH_3-SCR reaction [26]. Herein, we also investigated the influence of oxygen concentration on the NO_x conversion at fixed temperatures (200 and 300 °C). As shown in Fig. 6, only 10 and 40% NO_x conversions were obtained in the absence of O_2 at 200 and 300 °C, respectively. This is probably due to the occurrence of the following reaction: $6NO + 4NH_3 \rightarrow 5N_2 + 6H_2O$. With the increasing of O_2 concentration in the reactants, the NO_x conversions showed monotonic increase at both 200 and 300 °C. The NO_x conversions
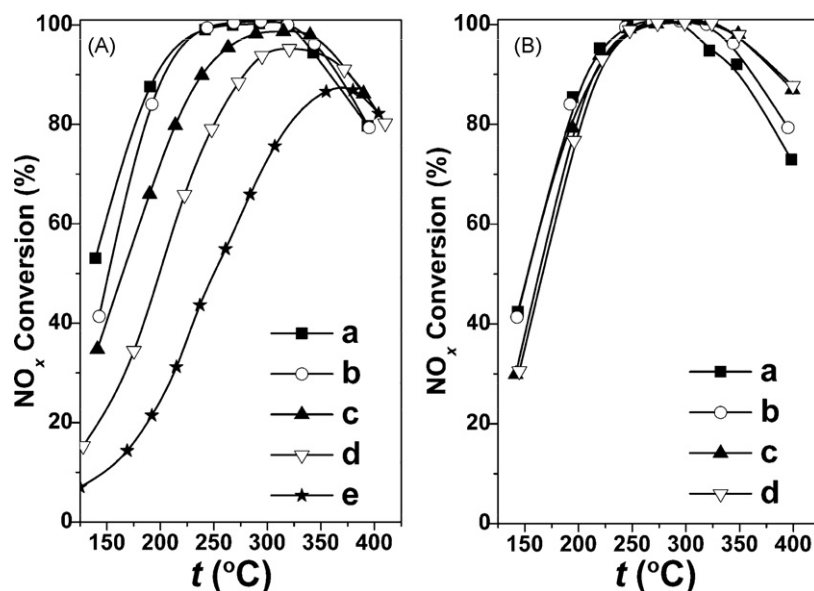

Fig. 5. NO_x conversion in the NH_3-SCR reaction over Fe_xTiO_y–$Ti(SO_4)_2$ under (A) different GHSV: (a)–(e) 25,000, 50,000, 80,000, 100,000 and 250,000 h^{-1}, other conditions: $[NO] = [NH_3] = 500$ ppm, $[O_2] = 5$ vol.% and N_2 balance; and (B) different reactant concentration: (a)–(d) $[NO] = [NH_3] = 200$, 500, 800 and 1000 ppm, $[O_2] = 2, 5, 8, 10$ vol.%, other conditions: GHSV = 50,000 h^{-1} and N_2 balance.
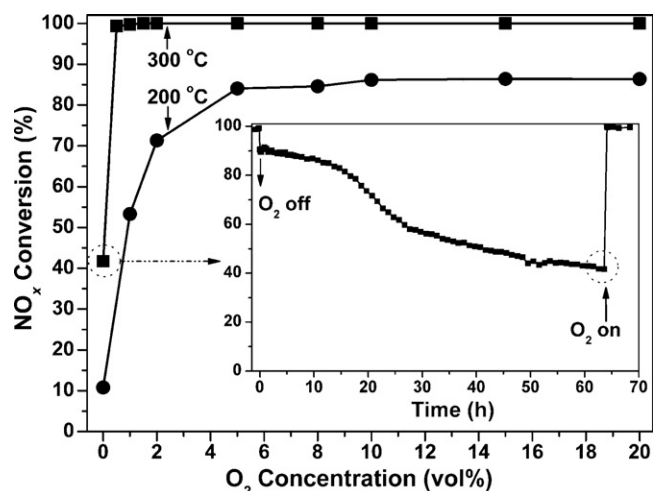
Fig. 6. Effect of O_2 concentration on the NO_x conversion over Fe_xTiO_y–$Ti(SO_4)_2$ at 200 and 300 °C. Reaction conditions: $[NO] = [NH_3] = 500$ ppm, $[O_2] = 0$–20 vol.%, N_2 balance and GHSV = 50,000 h^{-1}. Inset: NO_x conversion without O_2 as a function of time at 300 °C.

showed no decrease even at high O_2 concentration such as 15 and 20 vol.%, implying that under these reaction conditions the unselective oxidation of NH_3 to NO_x still did not occur resulting in high activity and N_2 selectivity in the SCR reaction. The inset in Fig. 6 shows the influence of O_2 on NO_x conversion when O_2 was cut off and recovered again at 300 °C. Interestingly, the NO_x conversion did not decline sharply to the minimum value but to 90% after the O_2 was cut off. And then, it took a long time (nearly 64 h) to decrease from 90 to 40%. The introduction of O_2 into the reactants again resulted in an immediate rebound of NO_x conversion to 100%. The same phenomenon has been also observed on Fe_2O_3–TiO_2 [9], Fe–Mn/TiO_2 [20] and Fe–Cr/TiO_2-pillared clay [27] catalysts, implying that not only the gas phase O_2 but also the lattice oxygen in this catalyst can participate in the SCR reaction.

3.2. Structural properties

3.2.1. N_2 physisorption

Fig. 7A shows the pore size distributions of Fe_xTiO_y–$Ti(SO_4)_2$, Fe_xTiO_y–$TiCl_4$ and Fe_2O_3/TiO_2. For comparison, Fe_2O_3 and TiO_2 were also analyzed and the results are shown in Fig. 7B. The BET
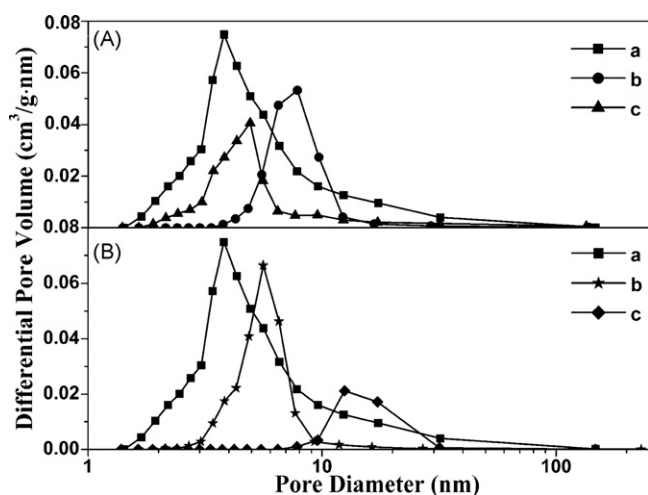

Fig. 7. Pore size distributions of (A) catalysts with different precursors: (a) Fe_xTiO_y–$Ti(SO_4)_2$, (b) Fe_xTiO_y–$TiCl_4$, and (c) Fe_2O_3/TiO_2; (B) iron titanate catalyst and pure oxides: (a) Fe_xTiO_y–$Ti(SO_4)_2$, (b) TiO_2, and (c) Fe_2O_3.
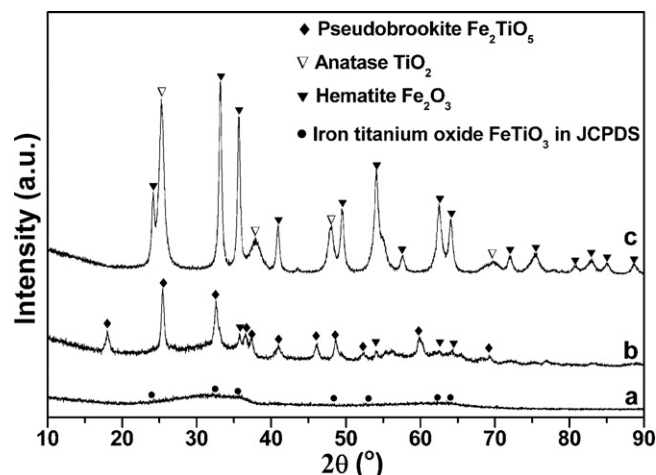

Fig. 8. Powder XRD patterns of (a) Fe_xTiO_y–$Ti(SO_4)_2$, (b) Fe_xTiO_y–$TiCl_4$, and (c) Fe_2O_3/TiO_2.

surface areas, BJH desorption pore volumes, average pore diameters together with the SCR reaction rates normalized by catalyst surface areas (R_S) are given in Table 1. Among the three catalysts, Fe_xTiO_y–$Ti(SO_4)_2$ had the largest surface area, the largest pore volume, the broadest pore size distribution and the smallest average pore diameter, which might be beneficial to the SCR reaction. It was also noticeable that the Fe_xTiO_y–$Ti(SO_4)_2$ catalyst possessed the most abundant micropores (<2 nm), supplying more inner surface area and active sites for the occurrence of SCR reaction. Normalized by the BET surface areas, the highest SCR reaction rates were also obtained over Fe_xTiO_y–$Ti(SO_4)_2$ at 150 and 200 °C. Compared with Fe_xTiO_y–$Ti(SO_4)_2$, the BET surface areas and pore volumes of Fe_xTiO_y–$TiCl_4$ and Fe_2O_3/TiO_2 were much smaller, and the average pore diameters were larger. The quantity of micropores in Fe_2O_3/TiO_2 was much smaller than that in Fe_xTiO_y–$Ti(SO_4)_2$, and there was nearly no micropores existing in Fe_xTiO_y–$TiCl_4$. Simultaneously, the SCR reaction rates over Fe_xTiO_y–$TiCl_4$ and Fe_2O_3/TiO_2 were also slower than that of Fe_xTiO_y–$Ti(SO_4)_2$. Pristine Fe_2O_3 and TiO_2 showed a poor SCR activity as shown in Table 1. Both of them had much smaller surface area and pore volume, and no obvious micropores were observed. Especially, the average pore diameter of Fe_2O_3 was as large as 19.4 nm.

3.2.2. Powder XRD

Powder XRD patterns of Fe_xTiO_y–$Ti(SO_4)_2$, Fe_xTiO_y–$TiCl_4$ and Fe_2O_3/TiO_2 are shown in Fig. 8. Fe_xTiO_y–$Ti(SO_4)_2$ showed no obvious sharp diffraction peaks besides some broad bumps, implying that this catalyst was mainly in the form of iron titanate crystallites ($FeTiO_3$ crystallite according to JCPDS card and Fe_2TiO_5 crystallite), which were thought to be the real active phases [11]. For Fe_xTiO_y–$TiCl_4$, better crystallization occurred during the calcination procedure. Pseudobrookite Fe_2TiO_5 existed in this sample and a small amount of hematite Fe_2O_3 also separated out, resulting in a smaller degree of porosity and a decrease of the active phases. For Fe_2O_3/TiO_2, only the XRD patterns of hematite Fe_2O_3 and anatase TiO_2 were observed.

3.2.3. UV–vis DRS

The results of UV–vis DRS experiments are shown in Fig. 9. As it is known, anatase TiO_2 usually shows an absorption threshold at 408 nm and an $O^{2-} \rightarrow Ti^{4+}$ charge-transfer band centered at 325 nm which can also be seen in Fig. 9A (a). Interestingly, an absorption band near 425 nm was also observed probably due to the existence of dopant energy level caused by the sulfate remained in TiO_2 lattice. Pure Fe_2O_3 showed a main band centered at 533 nm along

Table 1
Structural characterization of samples and SCR reaction rates normalized by catalyst surface areas.

Samples	S_{BET}[a] ($m^2\,g^{-1}$)	Pore volume[b] ($cm^3\,g^{-1}$)	Pore diameter[c] (nm)	R_S[d] $\times 10^{10}$ ($mol\,s^{-1}\,m^{-2}$)	
				150 °C	200 °C
Fe_xTiO_y–$Ti(SO_4)_2$	245.3	0.52	8.3	9.20	16.56
Fe_xTiO_y–$TiCl_4$	101.7	0.29	10.9	5.37	14.92
Fe_2O_3/TiO_2	92.1	0.28	12.1	3.41	15.93
TiO_2	103.5	0.20	7.6	0	0
Fe_2O_3	42.5	0.21	19.4	3.65	8.21

[a] BET surface area.
[b] BJH desorption pore volume.
[c] Average pore diameter.
[d] SCR reaction rates normalized by catalyst surface area.

with a shoulder band near 420 nm, which were the characteristics for iron oxide. A negative band at 746 nm indicated the presence of large Fe_2O_3 particles which was also observed in previous studies [28,29]. For Fe_xTiO_y–$Ti(SO_4)_2$, the interaction between iron and titanium shifted the absorption bands by about 70 nm towards visible light region comparing with those of TiO_2. No absorption band (especially the negative band at 746 nm) of Fe_2O_3 was detected implying that iron was in highly dispersive state, not aggregated large iron oxide particles in this sample. Fig. 9B shows the comparative absorption curves of Fe_xTiO_y–$Ti(SO_4)_2$, Fe_2O_3/TiO_2 and Fe_xTiO_y–$TiCl_4$. Obviously, not only the bands at 422 and 530 nm but also the symbol negative band at 746 nm existed in Fe_2O_3/TiO_2 and Fe_xTiO_y–$TiCl_4$, implying the presence of large iron oxide aggregates.

3.2.4. Raman spectroscopy

Visible Raman spectra in Fig. 10A show that TiO_2 and Fe_2O_3 displayed typical Raman shifts of anatase (E_g at 144, 197, 639 cm^{-1}, B_{1g} at 399 cm^{-1} and A_{1g} at 519 cm^{-1}) [30] and hematite (bands with arrowheads: A_{1g} at 227 cm^{-1}, E_g at 293, 407, 613 cm^{-1} and two unknown vibration modes at 189, 357 cm^{-1}) [31]. The intense peak at 1310 cm^{-1} can be assigned to a two-magnon scattering which arises from the interaction of two magnons created on antiparallel close spin sites in antiferromagnetic hematite [31]. Similar as the negative absorption band in UV–vis DRS, the obvious Raman shifts around 144 and 1310 cm^{-1} can be used as the symbols of anatase and hematite, respectively. These two kinds of crystal phases were obviously present in Fe_2O_3/TiO_2 catalyst,

which is in accordance with the XRD results. Besides, a small band at 345 cm^{-1} that could be assigned to Fe_2TiO_5 [32] also occurred in Fe_2O_3/TiO_2. This implied that a small amount of Fe^{3+} entered the TiO_2 lattice to form iron-doped anatase, even though XRD and UV–vis DRS could not give information about this. The XRD patterns of Fe_xTiO_y–$TiCl_4$ already revealed the existence of Fe_2TiO_5 and Fe_2O_3, and visible Raman spectra in Fig. 10A (d) confirmed this again. Bands at 205, 227, 345 and 667 cm^{-1} in Fe_xTiO_y–$TiCl_4$ are attributed to pseudobrookite Fe_2TiO_5 (corresponding vibration modes were not found in reported literature) [32,33] and the symbol band at 1310 cm^{-1} indicates the presence of hematite. For Fe_xTiO_y–$Ti(SO_4)_2$, the broadness of the Raman peaks was mainly due to the lattice defects, oxygen vacancies and poor crystallization [34]. Bands of crystallite Fe_2TiO_5 (205 and 345 cm^{-1}) also existed in this catalyst and other broad bands located at 176 (unknown vibration modes), 229 (E_g), 265 (A_g), 364 (A_g), and 689 (A_g) cm^{-1} could be assigned to crystallite $FeTiO_3$ [11,35]. No band around 1310 cm^{-1} belonging to Fe_2O_3 was detected, implying that no large iron oxide particles existed. However, the Raman shifts at 357 and 407 cm^{-1} still showed the presence of some Fe_2O_3 particles, maybe with very small grain sizes in bulk phase. The majority of iron species in this sample was in highly dispersive state, which is in accordance with XRD and UV–vis DRS results.

UV Raman spectra of titanium-containing samples are more surface-sensitive than visible Raman spectra [36]. In Fig. 10B, TiO_2 and Fe_2O_3 also showed typical Raman active modes of anatase (E_g at 144, 196, 640 cm^{-1}, B_{1g} at 398 cm^{-1} and A_{1g} at 518 cm^{-1}) and
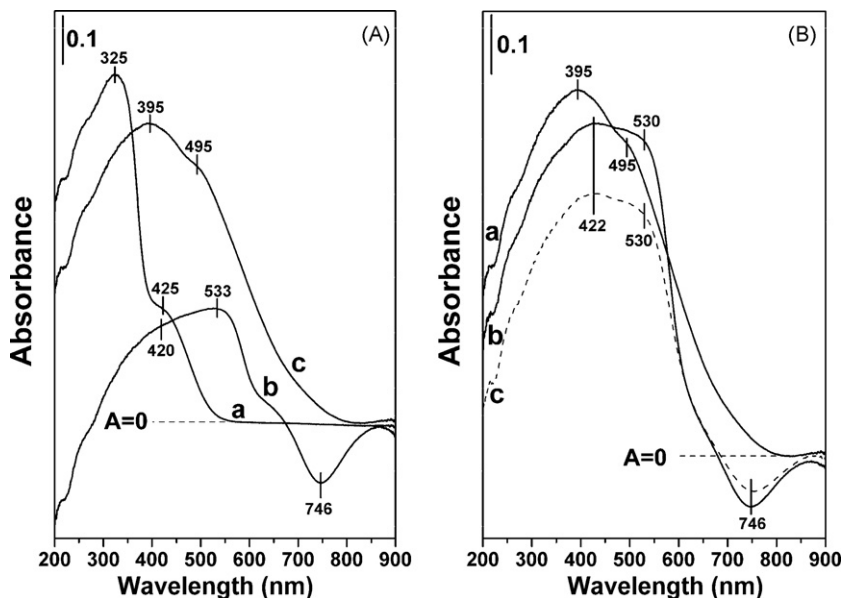

Fig. 9. UV–vis DRS results of (A) pure oxides and iron titanate catalyst: (a) TiO_2, (b) Fe_2O_3, and (c) Fe_xTiO_y–$Ti(SO_4)_2$; (B) catalysts with different precursors: (a) Fe_xTiO_y–$Ti(SO_4)_2$, (b) Fe_2O_3/TiO_2, and (c) Fe_xTiO_y–$TiCl_4$.

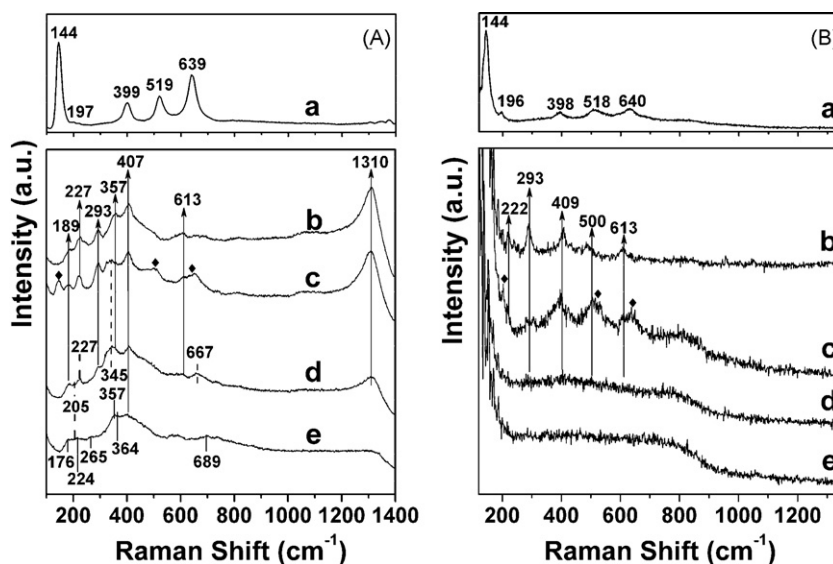**Fig. 10.** (A) Visible Raman spectra (λ_{ex} = 532 nm) and (B) UV Raman spectra (λ_{ex} = 325 nm) of (a) TiO_2, (b) Fe_2O_3, (c) Fe_2O_3/TiO_2, (d) Fe_xTiO_y–$TiCl_4$, and (e) Fe_xTiO_y–$Ti(SO_4)_2$; rhombic symbols denote anatase TiO_2.

hematite (bands with arrowheads), respectively. The symbol band of Fe_2O_3 in visible Raman spectra around 1310 cm^{-1} did not appear in UV Raman spectra, and we can identify the existence of iron oxide in other samples with the bands at 222, 500 cm^{-1} (A_{1g}) and 293, 409, 613 cm^{-1} (E_g). For Fe_2O_3/TiO_2 catalyst, the surface was mainly covered by hematite Fe_2O_3 and only weak bands of anatase TiO_2 (bands with rhombic symbols) were detected. This result is in accordance with the SEM and EDX results (Supporting Information, Fig. S2). Because of the strong absorption of UV light and the small size of oxides, the Raman scattering bands of Fe_xTiO_y–$TiCl_4$ and Fe_xTiO_y–$Ti(SO_4)_2$ were broadened to large bumps. The spectra of Fe_xTiO_y–$TiCl_4$ showed slight bands at the location of hematite, implying that the size of iron oxide particles in this sample were much smaller than those in Fe_2O_3/TiO_2. For Fe_xTiO_y–$Ti(SO_4)_2$, no additional bands of hematite or anatase existed except for a large bump from 200 to 800 cm^{-1}, proving that the surface of this catalyst was more homogeneous than those of other catalysts. In the following sections, we chose Fe_xTiO_y–$Ti(SO_4)_2$ as model catalyst to carry on XAFS study and redox behavior characterizations.

3.2.5. XAFS

XAFS can be used to determine the local environment around specific atoms, irrespective of crystallinity or dimensionality of the target materials. Fig. 11A and 11B present the normalized XANES and FT-EXAFS results of Fe K-edge in Fe_2O_3 and Fe_xTiO_y–$Ti(SO_4)_2$, respectively. In Fig. 11A, both of Fe_2O_3 and Fe_xTiO_y–$Ti(SO_4)_2$ had a characteristic pre-edge peak at 7114 eV indicated by dashed ellipse which could be ascribed to the 1s–3d dipolar forbidden transition [37]. The intensity of this peak in Fe_xTiO_y–$Ti(SO_4)_2$ was higher than that in Fe_2O_3. It has been reported that this 1s–3d dipolar forbidden transition would get additional intensity when the iron center was in a noncentral symmetric environmental or through mixing of 3d and 4p orbitals, which was caused by the breakdown of inversion symmetry because of the structure distortion [37]. Accordingly, we can deduce that, the interaction between iron and titanium species led to the structure distortion from sixfold coordination in Fe_2O_3 to fivefold or fourfold coordination in Fe_xTiO_y–$Ti(SO_4)_2$. The peak-fitting results of Fe K pre-edge peaks by searching for the optimum combination of Gaussian bands with the correlation coefficients (r^2) above 0.99 (PeakFit, Version 4.12, SeaSolve Software Inc.) were shown in the inset of Fig. 11A. By comparing the peak shape and peak position with literature data, the deconvolution sub-bands of Fe K pre-edge peak in Fe_2O_3 corresponded well with those of sixfold coordinated Fe^{3+} model compounds [38,39], and the single Gaussian band of Fe K pre-edge peak in Fe_xTiO_y–$Ti(SO_4)_2$ was in accordance with those of fivefold coordinated model compounds also with the iron species in the oxidation state of Fe^{3+} [38]. Furthermore, the adsorption edge position of Fe K-edge in Fe_xTiO_y–$Ti(SO_4)_2$ was calculated to be 7123.8 eV, which was 0.5 eV higher than that in Fe_2O_3 (7123.3 eV). The shift of adsorption edge position towards higher energy implied that the iron species in Fe_xTiO_y–$Ti(SO_4)_2$ showed higher oxidative ability than that in bulk iron oxides, which was probably caused by the deviation of electron cloud from Fe^{3+} to Ti^{4+}. The change in oxidative ability of iron species can be further proved by the XPS results, which will be presented later. For the FT-EXAFS results in Fig. 11B, Fe_2O_3 showed two characteristic peaks assigned to the Fe–O and Fe–O–Fe shells together with an obvious shoulder peak, which was also typical for α-Fe_2O_3. Besides the peak due to Fe–O shell, another peak ascribed to Fe–O–Ti [40,41] also appeared in Fe_xTiO_y–$Ti(SO_4)_2$, implying that the iron species in this catalyst was mainly in the form of highly isolated Fe^{3+}.

Fig. 11C shows the normalized XANES results of Ti K-edge in TiO_2 and Fe_xTiO_y–$Ti(SO_4)_2$. TiO_2 showed three small pre-edge peaks attributed to the transitions from the 1s core level of Ti to three different kinds of molecular orbitals ($1t_{1g}$, $2t_{2g}$ and $3e_g$) [42], which were typical for anatase with a sixfold coordination. Similar to the XANES results of Fe K-edge, Fe_xTiO_y–$Ti(SO_4)_2$ also had a pre-edge peak with a higher intensity than those in TiO_2, suggesting a structure distortion from sixfold coordination to fivefold or fourfold coordination. The same phenomenon was also observed in Fe_xO_y@Ti-HMS catalyst [43] because of the interaction between iron and titanium species. The FT-EXAFS results of Ti K-edge in TiO_2 and Fe_xTiO_y–$Ti(SO_4)_2$ are shown in Fig. 11D. For TiO_2, the peaks suggestive of Ti–O and contiguous Ti–O–Ti were observed. Comparatively, the first peak for Fe_xTiO_y–$Ti(SO_4)_2$ belonged to the Ti–O shell and the second one around 2.5 Å could be ascribed to Ti–O–Fe shell, implying again the formation of iron titanate crystallite. Comparatively, the Fe K-edge and Ti K-edge XAFS of Fe_xTiO_y–$Ti(SO_4)_2$ catalyst after activity test was also analyzed, as shown in Fig. S3. No obvious change of XANES and FT-EXAFS characteristics was observed, indicating that the structure of iron titanate crystallite was relatively stable under the SCR reaction condition.
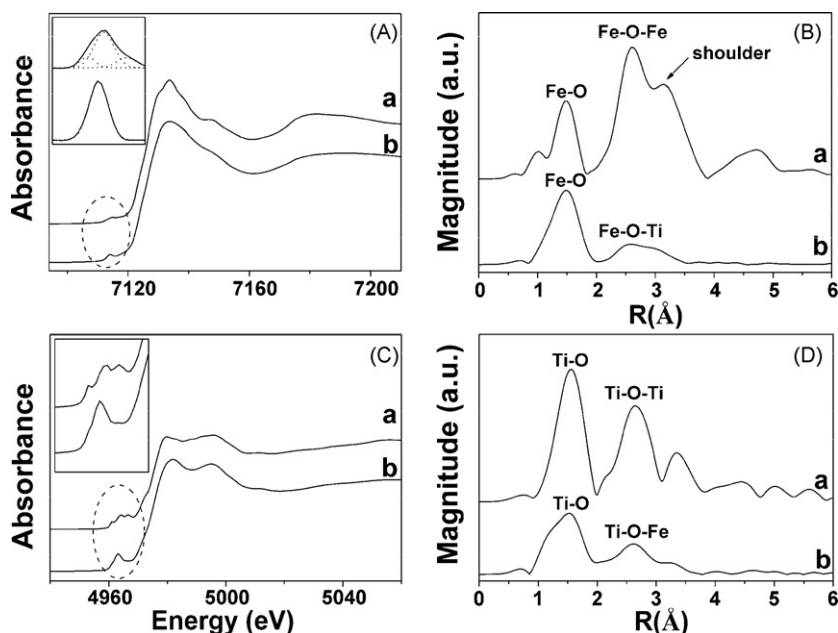
Fig. 11. (A) XANES and (B) FT-EXAFS results of Fe K-edge in (a) Fe_2O_3 and (b) Fe_xTiO_y–$Ti(SO_4)_2$; (C) XANES and (D) FT-EXAFS results of Ti K-edge in (a) TiO_2 and (b) Fe_xTiO_y–$Ti(SO_4)_2$.

Table 2
Fitted structural parameters for Fe_2O_3, TiO_2 and Fe_xTiO_y–$Ti(SO_4)_2$.

Samples	Coordination shell	Bond length (Å)	Coordination number	$\sigma \times 10^2$ (Å)
Fe_2O_3	Fe–O	2.06	4.0	10.4
		1.94	1.6	4.1
TiO_2	Ti–O	1.96	6.0	5.1
Fe_xTiO_y–$Ti(SO_4)_2$	Fe–O	1.95	4.7	8.3
	Ti–O	1.95	4.2	10.1

The fitted structural parameters by least-square method for Fe_2O_3, TiO_2 and Fe_xTiO_y–$Ti(SO_4)_2$ using α-Fe_2O_3, anatase TiO_2 and Fe_2TiO_4 as reference materials are shown in Table 2. Both of the Fe–O and Ti–O coordination numbers in Fe_xTiO_y–$Ti(SO_4)_2$ were indeed smaller that those in Fe_2O_3 and TiO_2, resulting in much more oxygen vacancies which were beneficial to the SCR reaction [44].

3.3. Redox behaviors

3.3.1. H_2-TPR

To investigate the reducibility of Fe_xTiO_y–$Ti(SO_4)_2$, H_2-TPR experiments were conducted using TiO_2 and Fe_2O_3 as reference materials and the results are shown in Fig. 12. TiO_2 had no obvious H_2 consumption peaks during the whole temperature range, therefore all the peaks present in Fig. 12(b) and (c) could be ascribed to the reduction of iron species. For Fe_2O_3 in Fig. 12(b), an obvious reduction peak below 500 °C and another large broad peak around 725 °C appeared. According to the calculated H_2/Fe molar ratio in the rectangle region, the former peak is attributed to the reduction from Fe_2O_3 to Fe_3O_4, during which the H_2/Fe molar ratio should be 0.17. The latter large broad peak in the high temperature range is due to the further reduction from Fe_3O_4 to FeO and partial Fe^0. For Fe_xTiO_y–$Ti(SO_4)_2$ in Fig. 12(c), obvious overlapped broad reduction peaks in the range of 300–500 °C appeared, and no reduction peak at higher temperatures was observed. The H_2-TPR profile of Fe_xTiO_y–$Ti(SO_4)_2$ had been tested for several times to confirm that the characteristics of the overlapped peaks below 500 °C was reproducible, as shown in Fig. S4. The H_2/Fe molar ratio in the rectangle region was calculated to be 0.52, indicating that all iron species in this sample was reduced from Fe^{3+} to Fe^{2+} below 500 °C. The overlapped reduction peaks were deconvoluted into four sub-bands by searching for the optimum combination of Gaussian bands with the correlation coefficients (r^2) above 0.99 and named as T_1, T_2, T_3 and T_4 from low to high temperatures (as shown in the inset). As the Fe^{3+} species showed nearly homogeneous dispersion on the surface of Fe_xTiO_y–$Ti(SO_4)_2$ catalyst and also in the bulk phase, as indicated by the above-mentioned characterization methods, it was reasonable to ascribe the different
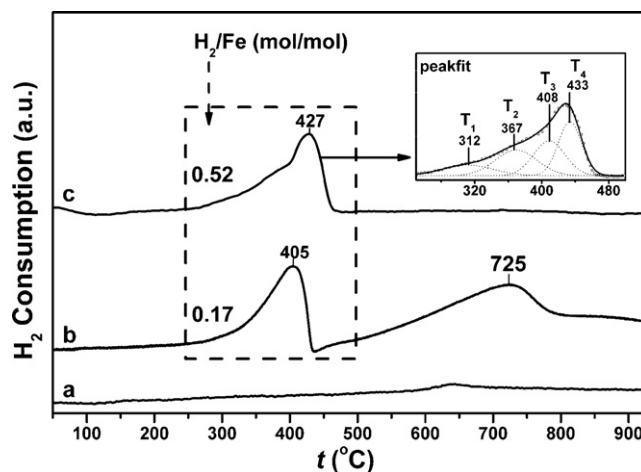

Fig. 12. H_2-TPR profiles of (a) TiO_2, (b) Fe_2O_3, and (c) Fe_xTiO_y–$Ti(SO_4)_2$.
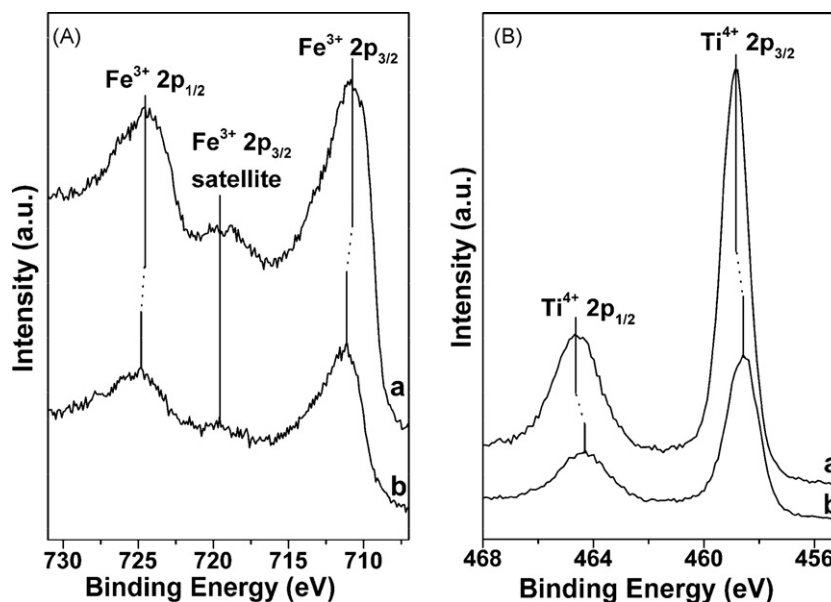
Fig. 13. XPS results of (A) Fe 2p in (a) Fe_2O_3 and (b) Fe_xTiO_y–$Ti(SO_4)_2$; (B) Ti 2p in (a) TiO_2 and (b) Fe_xTiO_y–$Ti(SO_4)_2$.

deconvoluted peaks to the progressive degrees of Fe^{3+} reduction, but not the reduction of Fe^{3+} species in different dispersive states. The T_1 sub-band is attributed to the reduction of surface adsorbed oxygen and the T_2 sub-band is assigned to the reduction of lattice oxygen from Fe^{3+}–O–Ti to $Fe^{2+/3+}$–O–Ti with intermediate valence as that in Fe_3O_4. The T_3 and T_4 sub-bands are attributed to the further reduction of lattice oxygen from $Fe^{2+/3+}$–O–Ti to Fe^{2+}–O–Ti at surface and inner layers, respectively. For the standard reduction process from Fe^{3+} to $Fe^{2+/3+}$ and then to Fe^{2+}, the area ratio of the two H_2 consumption peaks should be 1:2. Over Fe_xTiO_y–$Ti(SO_4)_2$, the area ratio of $T_2/(T_3 + T_4)$ was calculated to be 1:2.2, indicating that all Fe^{3+} species was indeed reduced to Fe^{2+} in this process, which is in well accordance with the H_2/Fe molar ratio result above. Due to the coexistence of iron and titanium species in Fe_xTiO_y–$Ti(SO_4)_2$, the reducibility of the iron titanate catalyst is totally different from that of bulk Fe_2O_3, which will be discussed later.

3.3.2. XPS

The XPS results are shown in Fig. 13. For Fe_2O_3 in Fig. 13A (a), the binding energies of Fe $2p_{3/2}$ (710.8 eV), Fe $2p_{1/2}$ (724.5 eV) together with the Fe $2p_{3/2}$ satellite peak corresponded well with Fe^{3+} [44,45]. The surface iron atomic concentration over Fe_2O_3 was calculated to be 23.1%. For Fe_xTiO_y–$Ti(SO_4)_2$ in Fig. 13A (b), the intensities of these Fe 2p peaks were much lower because of the decrease of iron concentration on the surface (9.5%). However, a slight increase in binding energies of these peaks was observed with Fe $2p_{3/2}$ shifting to 711.1 eV and Fe $2p_{1/2}$ shifting to 724.9 eV. This implied that the surface iron species in this sample showed more severe deviation of electron cloud by interacting with titanium species [44,45], leading to an enhancement in oxidative ability. This result is in well accordance with the XANES spectra of Fe K-edge in Fig. 11A.

In general, according to the law of conservation of charge, a binding energy increase of one element must be accompanied by a binding energy decrease of another element in an isolated system. Therefore, we can speculate that the titanium species in Fe_xTiO_y–$Ti(SO_4)_2$ might have a lower binding energy than that in TiO_2. The two intensive peaks of TiO_2 in Fig. 13B (a) at 458.9 and 464.7 eV could be attributed to Ti $2p_{3/2}$ and Ti $2p_{1/2}$, respectively, which are characteristics of Ti^{4+} [44]. As we expected in Fig. 13B

Table 3
Comparison of SCR performance over Fe_xTiO_y–$Ti(SO_4)_2$, V_2O_5–WO_3/TiO_2, Cu/ZSM-5 and Fe-containing zeolite catalysts in literature.

Samples	TOF ($\times 10^{-3}$ s^{-1})		
	150 °C	200 °C	250 °C
Fe_xTiO_y–$Ti(SO_4)_2$[a]	0.55	1.07	1.19
V_2O_5–WO_3/TiO_2[a]	0.25	1.00	3.50
Commercial Fe-exchanged BEA[a]	0.37	0.99	1.60
0.25Fe/HBEA[a]	3.00	8.50	17.00
Fe/ZSM-5[b]	–	ca. 8.00	ca. 24.50
Cu/ZSM-5[c]	9.34	20.30	20.30

[a] The number of active iron sites over Fe_xTiO_y–$Ti(SO_4)_2$ in TOF calculation was estimated from XPS (surface atomic concentration) and BET surface area data. According to our previous study [11], the BET surface area of Fe_xTiO_y-500 °C was nearly 60% of that of Fe_xTiO_y-400 °C, yet similar apparent SCR activity was obtained over these two samples. Therefore, in this study it was assumed that ca. 60% of surface area over Fe_xTiO_y–$Ti(SO_4)_2$ catalyst was effective in the real SCR reaction. The TOF data of V_2O_5–WO_3/TiO_2, commercial Fe-exchanged BEA and 0.25Fe/HBEA were obtained directly from [24]. Reaction conditions: [NO] = [NH$_3$] = 500 ppm, [O$_2$] = 5 vol.%, N$_2$ balance and GHSV = 50,000 h^{-1}.
[b] The TOF data of Fe/ZSM-5 were read directly from Fig. 14 in [47]. Reaction conditions: [NO] = [NH$_3$] = 1000 ppm, [O$_2$] = 8 vol.%, [CO$_2$] = 10 vol.%, [H$_2$O] = 8 vol.%, N$_2$ balance and W/F = 0.2 gl/min.
[c] The TOF data of Cu/ZSM-5 were calculated with the best SCR result over CuZSM5-124-fresh sample in [48]. Reaction conditions: [NO] = [NH$_3$] = 500 ppm, [O$_2$] = 5 vol.%, [H$_2$O] = 10 vol.%, N$_2$ balance and GHSV = 100,000 h^{-1}.

(b), the binding energies of Ti $2p_{3/2}$ and Ti $2p_{1/2}$ in Fe_xTiO_y–$Ti(SO_4)_2$ indeed had a decrease which shifted to 458.6 and 464.4 eV, respectively, indicating that the titanium species in this catalyst had higher density of electron cloud than that in TiO_2.

4. Discussion

4.1. Catalytic performance

Activity test results in Fig. 1 showed that catalyst precursors ($Ti(SO_4)_2$ versus $TiCl_4$) and preparation methods (co-precipitation versus impregnation) indeed had obvious influence on the NH$_3$-SCR activity, including the NO$_x$ conversion and N$_2$ selectivity. The difference of NO oxidation activity (Fig. 2A) and NH$_3$ oxidation activity (Fig. 2B) over these catalysts was one of the reasons for the SCR activity discrepancy. The Fe_xTiO_y–$Ti(SO_4)_2$ catalyst possessed highest NO oxidation activity in the low temperature

range and moderate NH_3 oxidation activity in the high temperature range, leading to an excellent SCR activity and N_2 selectivity during the whole temperature range that we investigated. It is noticeable that the Fe_xTiO_y–$Ti(SO_4)_2$ catalyst showed a good activity in the specific temperature window of 200–350 °C with the NO_x conversion above 90% in the absence of H_2O, which was 50–150 °C lower than those of Fe/ZSM-5 [6,15,46], Fe–TiO_2-PILC [7], Fe_2O_3/WO_3/ZrO_2 [8] or Fe/HBEA zeolite catalysts [24]. The increase of NO_2 inlet concentration could significantly promote the low temperature activity and further enlarge the operation temperature window.

For comparing the catalytic performance of Fe_xTiO_y–$Ti(SO_4)_2$ with other commercial or reported SCR catalysts, the turnover frequencies (TOF, 10^{-3} s^{-1}) of NO_x at 150, 200 and 250 °C were estimated and listed in Table 3. The TOF data of NO_x over Fe_xTiO_y–$Ti(SO_4)_2$ might be rough because the accurate number of effective iron atoms exposed on the surface was difficult to obtain, especially for this iron titanate catalyst with a majority of ineffective iron species in the bulk phase. However, based on the XPS (surface atomic concentration) and BET surface area data to determine the surface iron sites, the magnitude of the TOF data should be right and useful. As we can see, the intrinsic activity of Fe_xTiO_y–$Ti(SO_4)_2$ is comparable to that of the state-of-the-art SCR catalyst V_2O_5–WO_3/TiO_2 or commercial Fe-exchanged BEA catalyst, but still much lower than that of Fe/HBEA, Fe/ZSM-5 or Cu/ZSM-5 reported by other researchers [24,47,48]. In our future work, we can optimize the catalyst composition or prepare washcoated monolith catalyst using Fe_xTiO_y–$Ti(SO_4)_2$ as active component to further enhance its intrinsic activity.

Over our best iron titanate catalyst Fe_xTiO_y–$Ti(SO_4)_2$, as shown in Fig. 5A, the NO_x conversion was sensitive to the contact time, thus the GHSV is an important factor needed to be considered in designing preformed catalyst for industrial application. The experimental results in Fig. 5B showed that this iron titanate catalyst had a good performance under high reactant concentration, which is beneficial to the actual utilization. Like previous study showed [26], O_2 can also significantly promote the SCR reaction over Fe_xTiO_y–$Ti(SO_4)_2$ (Fig. 6). This is possibly owing to the enhancement of NO oxidation by O_2 through which the "fast SCR" can take place, or the reoxidation of active sites by O_2 to complete a redox cycle. The XPS results of Fe_xTiO_y–$Ti(SO_4)_2$ after 64 h reaction at 300 °C under NO + NH_3 atmosphere (Supporting Information, Fig. S5) showed that both of the Fe $2p_{3/2}$ and Fe $2p_{1/2}$ peaks shifted towards lower binding energies, indicating a lower oxidation state of iron species due to the consumption of lattice oxygen. This point of view could also be directly verified by the catalyst surface color changing from brown to light black due to the reduction of partial Fe^{3+} to Fe^{2+}. This implies that O_2 is indeed very necessary to reoxidize Fe^{2+} to Fe^{3+} in the SCR reaction; otherwise, the physico-chemical property of catalyst will be slowly changed in the absence of O_2. The promotion effect of O_2 in SCR reaction will also be discussed in the successive series of this study.

The durability of SO_2/H_2O over the Fe_xTiO_y–$Ti(SO_4)_2$ catalyst has been tested at 300 °C in our previous work [11]. When 100 ppm SO_2 and (or) 10 vol.% H_2O were added into the reactants, the NO_x conversion could maintain at 100% for a 48 h test. No degradation of catalytic activity of Fe_xTiO_y–$Ti(SO_4)_2$ catalyst was observed at the fixed temperature. Even after 48 h sulfation, the catalyst still showed NO_x conversion above 90% from 250 to 400 °C. As the Fe_xTiO_y–$Ti(SO_4)_2$ catalyst was prepared at 400 °C with long-time (6 h) calcination, its structure property and catalytic activity would be stable if the reaction temperature was below 400 °C in practical use. Excellent NH_3-SCR activity, N_2 selectivity and SO_2/H_2O durability in a broad medium temperature range make this iron titanate catalyst a potential candidate for industrial application.

4.2. Structural properties and active phase

During the preparation procedure, intense hydrolysis of $TiCl_4$ usually occurred if no ice-water bath was used and this made it difficult in controlling the final composition of Fe_xTiO_y–$TiCl_4$. There was no such problem when using $Ti(SO_4)_2$ as Ti precursor. Furthermore, anion species (Cl$^-$ and SO_4^{2-}) contained in the precursors might be another important factor influencing the catalyst structure and morphology. Theoretically, SO_4^{2-} has stronger coordinating effect with metal ions comparing with Cl$^-$, so the former anion is more difficult to be removed completely during the washing process. Moreover, SO_4^{2-} has cubic structure with larger volume, whereas, Cl$^-$ is only an ion dot [49]. The residual SO_4^{2-} can induce lattice defects into the mixed oxides, while the effect of Cl$^-$ is not so obvious. It was reported [50,51] that a small amount of SO_4^{2-} existing in anatase TiO_2 lattice could strongly hinder the crystallization and phase transformation to rutile TiO_2, thus leading to an increase in the surface area and pore volume, as the results shown in Table 1. Only after high temperature calcination (such as 600 or 700 °C), the crystallization of Fe_xTiO_y–$Ti(SO_4)_2$ was enhanced to form pseudobrookite Fe_2TiO_5 and partial rutile TiO_2 [11], in contrast to the formation of well-crystallized Fe_2TiO_5 in Fe_xTiO_y–$TiCl_4$ after calcination at as low as 400 °C (Fig. 8). It was reported that the incorporation of SO_4^{2-} and other transition metal ions (Cr, Mn, Fe, Co, Ni, Cu and Zn) into the lattice could also enhance the surface acidity of anatase TiO_2 [52]. Therefore, it is suggested that the sulfate contained in $Ti(SO_4)_2$ precursor in this study also had a similar effect, resulting in the differences of surface area, pore volume, pore diameter, surface acidity and thus the SCR activity of these two catalysts.

XRD results in Fig. 8(a) and (b) confirmed the conclusion above. Fe_xTiO_y–$Ti(SO_4)_2$ was mainly in the form of iron titanate crystallites, which were thought to be the real active phases in the SCR reaction. Comparatively, pseudobrookite Fe_2TiO_5 and hematite Fe_2O_3 separated out in Fe_xTiO_y–$TiCl_4$ owing to the absence of sulfate as phase transformation inhibitor, resulting in a decrease in surface area, micropores and thus the SCR activity. For Fe_2O_3/TiO_2 prepared using impregnation method, the interaction between iron and titanium in atomic scale was not strong as those in iron titanate catalysts. The iron species was mainly in the form of hematite particles, as shown in Fig. 8(c). Therefore, the surface area and pore volume were the smallest and the pore diameter was the largest, resulting in a lower activity. Although previous studies [9,53] showed that Fe_2O_3 also had a good SCR activity, the catalytic performance of iron titanate crystallites was much better, especially for the low temperature activity and N_2 selectivity.

According to the UV–vis DRS results of TiO_2/Fe-MCM-41 from Reddy et al. [45], the absorption curve could be symbolically divided into three parts: the first part in 200–400 nm corresponded to the absorption by titania, the second part in 400–500 nm corresponded to the adsorption by iron-doped titania, and the third part in 500–600 nm corresponded to the absorption by iron oxide. Therefore, compared with the band near 425 nm in TiO_2 (Fig. 9A (a)), the lift-up of the curve near 495 nm in Fe_xTiO_y–$Ti(SO_4)_2$ (Fig. 9A (c)) was possibly due to the strong absorption of visible light by the new active phases (iron titanate crystallites with Fe–O–Ti structure) occurred in our catalyst. In order to further elucidate the existing states of iron species in different catalysts, we further deconvoluted the UV–vis DRS spectra searching for the optimum combination of Gaussian bands (Supporting Information, Fig. S6). Unlike the iron-containing catalysts reported by other researchers, such as Fe/HBEA [24] and Fe/ZSM-5 [47,54], of which the bare zeolite supports showed no obvious absorption in the whole wavelength range, the titanium species in our catalysts showed strong absorption, especially in the UV light
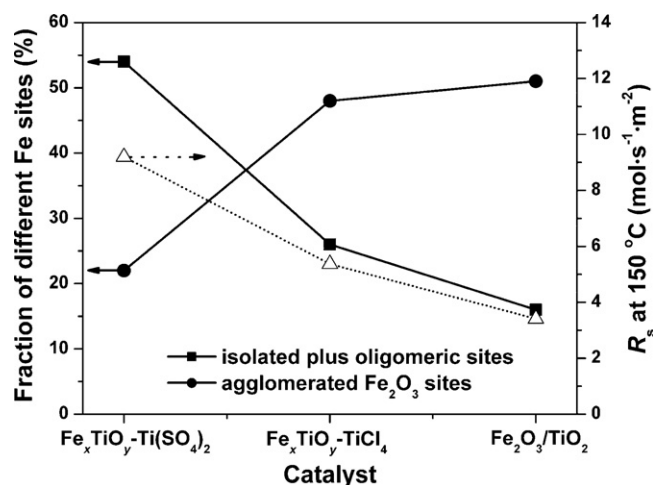
Fig. 14. Correlation between the fractions of different iron species and the SCR reaction rates at 150 °C normalized by surface areas over different catalysts.

range. Therefore, it is complicated to distinguish the isolated iron species from titanium species, both of which showed ligand to metal charge-transfer (LMCT) below 300 nm. Moreover, the absorption coefficients for LMCT bands of the titanium species and various iron species are unknown, so the deconvolution results are actually rough. However, we can still semiquantitatively estimate the fractions of isolated plus oligomeric iron sites and agglomerated Fe_2O_3 sites by calculating the sub-bands area ratio. Although the XRD results showed that there was no crystal Fe_2O_3 existing in Fe_xTiO_y–$Ti(SO_4)_2$, a small quantity of not-well-crystallized iron oxides still occurred according to the results in Fig. S6A. The correlation between the fractions of different iron species and the SCR reaction rates at 150 °C over different catalysts is shown in Fig. 14. As we can see, the SCR reaction rates have a positive correlation with the fraction of isolated plus oligomeric iron sites, and a negative correlation with the fraction of agglomerated Fe_2O_3 sites. Previous study by Balle et al. [24] showed that the SCR activity over Fe/HBEA decreased in the following sequence: isolated iron sites > oligomeric iron sites > agglomerated iron sites. Therefore, the highest SCR activity of Fe_xTiO_y–$Ti(SO_4)_2$ catalyst can be attributed to the most abundant isolated and oligomeric iron sites due to the strong interaction between iron and titanium species. The FTIR spectra of Fe_xTiO_y–$Ti(SO_4)_2$ (Supporting Information, Fig. S7) also showed multiple absorption of Fe–O, Ti–O and Fe–O–Ti groups in the wavelength range of 500–600 cm^{-1} (centered at 561 cm^{-1}), implying the formation of iron titanate crystallites with much more well-dispersed iron species.

Raman results in Fig. 10 directly showed that the Fe_xTiO_y–$Ti(SO_4)_2$ catalyst was mainly composed of $FeTiO_3$ and Fe_2TiO_5 crystallites besides of some small iron oxide particles, which is in accordance with the XRD, UV–vis DRS and FTIR absorption results. Iron species in Fe_xTiO_y–$Ti(SO_4)_2$, mainly in the form of isolated Fe^{3+}, was much more homogenous than those in Fe_xTiO_y–$TiCl_4$ and Fe_2O_3/TiO_2. XAFS results in Fig. 11 showed that the Fe–O and Ti–O coordination structures in Fe_xTiO_y–$Ti(SO_4)_2$ were different from those in Fe_2O_3 and TiO_2 bulk oxides, with smaller coordination numbers and larger structure distortion. The oxidative ability of iron species was also increased to a certain extent probably due to the deviation of electron cloud from Fe^{3+} to Ti^{4+}. The interaction between iron and titanium species in this catalyst led to a formation of homogeneous Fe–O–Ti structure with high activity in the SCR reaction.

4.3. Redox behaviors

The H_2-TPR results in Fig. 12 showed that below 500 °C, the iron species in Fe_xTiO_y–$Ti(SO_4)_2$ could be totally reduced from Fe^{3+} to Fe^{2+}; however, the bulk Fe_2O_3 could be only reduced to Fe_3O_4 until this temperature. Although it seems that the temperature of the maximum H_2 consumption rate over Fe_2O_3 is lower than that over Fe_xTiO_y–$Ti(SO_4)_2$, the reducibility of iron titanate catalyst is actually higher than that of bulk Fe_2O_3. This indicates that higher mobility of lattice oxygen is obtained over Fe_xTiO_y–$Ti(SO_4)_2$ due to the strong interaction between iron and titanium species, which is beneficial to enhance the oxidative ability and thus the SCR activity of iron titanate catalyst. Above 500 °C, a large proportion of the formed Fe^{2+}–O–Ti species over Fe_xTiO_y–$Ti(SO_4)_2$ could not be continuously reduced to Fe^0–O–Ti due to the formation of ilmenite or partial metallic iron covering the catalyst surface to block the H_2 diffusion into the inner layers. Due to the absence of titanium species in Fe_2O_3, the final reduction product could be metallic Fe^0 if the temperature was high enough. Summarizing the H_2-TPR results we can see that, the reducibility of iron species in Fe_xTiO_y–$Ti(SO_4)_2$ is different from that in bulk Fe_2O_3, owing to the formation of new active phases. The Fe^{3+} species in Fe_xTiO_y–$Ti(SO_4)_2$ is much easier to be reduced with higher oxidative ability than those in Fe_2O_3, which is in accordance with the XPS results in Fig. 13A.

The change of oxidative ability of titanium could not be determined from H_2-TPR results due to the absence of titanium reduction peaks, yet we can get some information from the XPS results in Fig. 13B. With the increasing of binding energies of Fe 2p, the binding energies of Ti 2p showed an obvious decrease, implying the possession of a higher density of electron cloud than that in TiO_2. The same phenomenon was also observed in other iron–titanium oxide composites [55,56] and the lowering of binding energies might be owing to the formation of Ti–O–Fe bond [55]. Moreover, we also measured the XPS spectra of Fe 2p and Ti 2p in Fe_xTiO_y–$TiCl_4$ and Fe_2O_3/TiO_2, and the results are shown in Fig. S8. Similar as the results in Fig. 13, the coexistence of iron and titanium species also led to higher binding energies of Fe^{3+} and lower binding energies of Ti^{4+}. Although other characterization methods showed that the iron species in Fe_2O_3/TiO_2 was mainly in the form of large aggregated iron oxides particles, a small part of iron species still had strong interaction with titanium species to form Fe–O–Ti structure. We speculate that this phenomenon may universally occur in iron–titanium-containing materials and the specific Fe–O–Ti structure is highly active in the SCR reaction.

Thus, the short conclusion can be drawn that the interaction between iron and titanium species resulted in a formation of iron titanate phase (Fe–O–Ti) which possessed different redox ability from those of pure oxides; the enhanced oxidative ability of Fe^{3+} species might be responsible for the high activity in the SCR reaction, during which the *in situ* oxidation of NO by O_2 over Fe^{3+} is very important.

5. Conclusions

Iron titanate catalyst (Fe_xTiO_y–$Ti(SO_4)_2$) prepared by conventional co-precipitation method using $Fe(NO_3)_3·9H_2O$ and $Ti(SO_4)_2$ as precursors showed excellent activity, N_2 selectivity and H_2O/SO_2 durability in the SCR of NO with NH_3 in the medium temperature range. This Fe_xTiO_y–$Ti(SO_4)_2$ catalyst showed a good SCR activity in the specific temperature window of 200–350 °C with the NO_x conversion above 90% in the absence of H_2O, which was 50–150 °C lower than those of other known Fe-based catalysts. O_2 played an important role to promote the SCR process, and some lattice oxygen in the catalyst could also take part in the reaction in the absence of gaseous O_2. Precursors and preparation methods had evident

influence on the structure and activity of iron titanate catalyst. According to the XRD, UV–vis DRS, Raman spectroscopy and EXAFS results, the active phase in Fe_xTiO_y–$Ti(SO_4)_2$ catalyst was mainly in the form of iron titanate crystallites with specific Fe–O–Ti structure, but not large aggregated iron oxide particles. XANES, H_2-TPR and XPS results showed that the interaction between iron and titanium species in this catalyst resulted in an enhancement of oxidative ability of Fe^{3+}, which was beneficial to the SCR reaction.

Acknowledgements

Appendix A. Supplementary data

Supplementary data associated with this article can be found, in the online version, at doi:10.1016/j.apcatb.2010.02.038.

References

[1] J.P. Dunn, P.R. Koppula, H.G. Stenger, I.E. Wachs, Appl. Catal. B: Environ. 19 (1998) 103.
[2] Vanadium Pentoxide; MSDS No. V2220; Mallinckrodt Baker: Phillipsburg, NJ, July 1, 2009. http://www.jtbaker.com/msds/englishhtml/v2220.htm (Accessed 1/20/10).
[3] G. Qi, R.T. Yang, J. Catal. 217 (2003) 434.
[4] P.G. Smirniotis, P.M. Sreekanth, D.A. Peña, R.G. Jenkins, Ind. Eng. Chem. Res. 45 (2006) 6436.
[5] W.S. Kijlstra, D.S. Brands, E.K. Poels, A. Bliek, J. Catal. 171 (1997) 208.
[6] R.Q. Long, R.T. Yang, J. Am. Chem. Soc. 121 (1999) 5595.
[7] R.Q. Long, R.T. Yang, J. Catal. 186 (1999) 254.
[8] N. Apostolescu, B. Geiger, K. Hizbullah, M.T. Jan, S. Kureti, D. Reichert, F. Schott, W. Weisweiler, Appl. Catal. B: Environ. 62 (2006) 104.
[9] A. Kato, S. Matsuda, F. Nakajima, M. Imanari, Y. Watanabe, J. Phys. Chem. 85 (1981) 1710.
[10] F. Nakajima, I. Hamada, Catal. Today 29 (1996) 109.
[11] F. Liu, H. He, C. Zhang, Chem. Commun. (2008) 2043.
[12] T. Ressler, J. Synchrotron Rad. 5 (1998) 118.
[13] M. Newville, J. Synchrotron Rad. 8 (2001) 322.
[14] F. Liu, H. He, Y. Ding, C. Zhang, Appl. Catal. B: Environ. 93 (2009) 194.
[15] M. Devadas, O. Kröcher, M. Elsener, A. Wokaun, N. Söger, M. Pfeifer, Y. Demel, L. Mussmann, Appl. Catal. B: Environ. 67 (2006) 187.
[16] G. Madia, M. Koebel, M. Elsener, A. Wokaun, Ind. Eng. Chem. Res. 41 (2002) 3512.
[17] A. Grossale, I. Nova, E. Tronconi, D. Chatterjee, M. Weibel, J. Catal. 256 (2008) 312.
[18] C. Ciardelli, I. Nova, E. Tronconi, D. Chatterjee, B. Bandl-Konrad, M. Weibel, B. Krutzsch, Appl. Catal. B: Environ. 70 (2007) 80.
[19] R.Q. Long, R.T. Yang, Appl. Catal. B: Environ. 27 (2000) 87.
[20] G. Qi, R.T. Yang, Appl. Catal. B: Environ. 44 (2003) 217.
[21] Z. Liu, P.J. Millington, J.E. Bailie, R.R. Rajaram, J.A. Anderson, Micropor. Mesopor. Mater. 104 (2007) 159.
[22] W.S. Kijlstra, D.S. Brands, H.I. Smit, E.K. Poels, A. Bliek, J. Catal. 171 (1997) 219.
[23] G.M. Underwood, T.M. Miller, V.H. Grassian, J. Phys. Chem. A 103 (1999) 6184.
[24] P. Balle, B. Geiger, S. Kureti, Appl. Catal. B: Environ. 85 (2009) 109.
[25] J.N. Armor, Catal. Today 38 (1997) 163.
[26] H. Bosch, F. Janssen, Catal. Today 2 (1988) 369.
[27] L.S. Cheng, R.T. Yang, N. Chen, J. Catal. 164 (1996) 70.
[28] M.S. Kumar, M. Schwidder, W. Grünert, A. Brückner, J. Catal. 227 (2004) 384.
[29] S. Bordiga, R. Buzzoni, F. Geobaldo, C. Lamberti, E. Giamello, A. Zecchina, G. Leofanti, G. Petrini, G. Tozzola, G. Vlaic, J. Catal. 158 (1996) 486.
[30] Y. Cong, J. Zhang, F. Chen, M. Anpo, D. He, J. Phys. Chem. C 111 (2007) 10618.
[31] D.L.A. de Faria, S. Venâncio Silva, M.T. de Oliveira, J. Raman Spectrosc. 28 (1997) 873.
[32] W.G. Menezes, P.H.C. Camargo, M.M. Oliveira, D.J. Evans, J.F. Soares, A.J.G. Zarbin, J. Colloid Interface Sci. 299 (2006) 291.
[33] P.H.C. Camargo, G.G. Nunes, G.R. Friedermann, D.J. Evans, G.J. Leigh, G. Tremiliosi-Filho, E.L. de Sá, A.J.G. Zarbin, J.F. Soares, Mater. Res. Bull. 38 (2003) 1915.
[34] N.V. Minh, D.H. Long, N.T. Khoi, Y. Jung, S.J. Kim, I.S. Yang, IEEE Trans. Nanotechnol. 7 (2008) 177.
[35] A. Wang, K.E. Kuebler, B.L. Jolliff, L.A. Haskin, Am. Mineral. 89 (2004) 665.
[36] J. Zhang, M. Li, Z. Feng, J. Chen, C. Li, J. Phys. Chem. B 110 (2006) 927.
[37] Y. Wang, Q. Zhang, T. Shishido, K. Takehira, J. Catal. 209 (2002) 186.
[38] P.-E. Petit, F. Farges, M. Wilke, V.A. Solé, J. Synchrotron Rad. 8 (2001) 952.
[39] G. Berlier, G. Spoto, S. Bordiga, G. Ricchiardi, P. Fisicaro, A. Zecchina, I. Rossetti, E. Selli, L. Forni, E. Giamello, C. Lamberti, J. Catal. 208 (2002) 64.
[40] X. Zhang, M. Zhou, L. Lei, Catal. Commun. 7 (2006) 427.
[41] H. Yamashita, M. Harada, J. Misaka, M. Takeuchi, B. Neppolian, M. Anpo, Catal. Today 84 (2003) 191.
[42] H. Yamashita, Y. Ichihashi, M. Anpo, M. Hashimoto, C. Louis, M. Che, J. Phys. Chem. 100 (1996) 16041.
[43] K. Mori, Y. Kondo, S. Morimoto, H. Yamashita, Chem. Lett. 36 (2007) 1068.
[44] S. Roy, B. Viswanath, M.S. Hegde, G. Madras, J. Phys. Chem. C 112 (2008) 6002.
[45] E.P. Reddy, L. Davydov, P.G. Smirniotis, J. Phys. Chem. B 106 (2002) 3394.
[46] G. Qi, R.T. Yang, Appl. Catal. B: Environ. 60 (2005) 13.
[47] M. Iwasaki, K. Yamazaki, K. Banno, H. Shinjoh, J. Catal. 260 (2008) 205.
[48] J.-H. Park, H.J. Park, J.H. Baik, I.S. Nam, C.-H. Shin, J.-H. Lee, B.K. Cho, S.H. Oh, J. Catal. 240 (2006) 47.
[49] G. Pecchi, P. Reyes, T. López, R. Gómez, A. Moreno, J.L.G. Fierro, J. Chem. Technol. Biotechnol. 77 (2002) 944.
[50] S. Yamazaki, N. Fujinaga, K. Araki, Appl. Catal. A: Gen. 210 (2001) 97.
[51] S.K. Samantaray, T. Mishra, K.M. Parida, J. Mol. Catal. A: Chem. 156 (2000) 267.
[52] K.R. Sunajadevi, S. Sugunan, Mater. Lett. 58 (2004) 3290.
[53] J.P. Chen, M.C. Hausladen, R.T. Yang, J. Catal. 151 (1995) 135.
[54] J. Pérez-Ramírez, J.C. Groen, A. Brückner, M.S. Kumar, U. Bentrup, M.N. Debbagh, L.A. Villaescusa, J. Catal. 232 (2005) 318.
[55] N. Perkas, O. Palchik, I. Brukental, I. Nowik, Y. Gofer, Y. Koltypin, A. Gedanken, J. Phys. Chem. B 107 (2003) 8772.
[56] A. Glisenti, J. Mol. Catal. A: Chem. 153 (2000) 169.